

EnKode: Active Learning of Unknown Flows with Koopman Operators

Alice K. Li¹, Thales C. Silva¹, and M. Ani Hsieh¹

Abstract—In this letter, we address the task of adaptive sampling to model vector fields. When modeling environmental phenomena with a robot, gathering high resolution information can be resource intensive. Actively gathering data and modeling flows with the data is a more efficient alternative. However, in such scenarios, data is often sparse and thus requires flow modeling techniques that are effective at capturing the relevant dynamical features of the flow to ensure high prediction accuracy of the resulting models. To accomplish this effectively, regions with high informative value must be identified. We propose EnKode, an active sampling approach based on Koopman Operator theory and ensemble methods that can build high quality flow models and effectively estimate model uncertainty. For modeling complex flows, EnKode provides comparable or better estimates of unsampled flow regions than Gaussian Process Regression models with hyperparameter optimization. Additionally, our active sensing scheme provides more accurate flow estimates than comparable strategies that rely on uniform sampling. We evaluate EnKode using three common benchmarking systems: the Bickley Jet, Lid-Driven Cavity flow with an obstacle, and real ocean currents from the National Oceanic and Atmospheric Administration (NOAA).

Index Terms—Environment Monitoring and Management; Dynamics; Active Sensing; Uncertainty Quantification; Koopman Operator Theory

I. INTRODUCTION

MODELING unknown fluid flow fields is fundamental for aerial and marine robotic applications including search and rescue, oil spill mitigation, and scientific discovery, to name a few [1]. However, obtaining accurate flow maps is challenging because data are difficult to acquire, and the physics of flows are not yet fully understood. Robots are increasingly being deployed to gather data to build better models [2]–[10]. As such, since obtaining data is difficult, there is an increasing need for effective flow models and active information-theoretic sampling strategies to improve flow estimation online.

Although there are works that use adaptive sampling to model flows online using sparse data gathered by robots [3], [4], we have not yet seen works that leverage Koopman theory. Koopman Operator Theory (KOT), discovered by B.O.

Manuscript received: June, 14, 2024; Revised September, 1, 2024; Accepted September, 29, 2024. This paper was recommended for publication by Editor-in-Chief Tamim Asfour and Editor Jens Kober upon evaluation of the Reviewers' comments. This work was supported by NSF IUCRC 1939132, NSF IIS 1910308, and the University of Pennsylvania's University Research Foundation Award

¹Alice K. Li, Thales C. Silva, and M. Ani Hsieh are with the General Robotics Actuation Sensing and Perception (GRASP) Laboratory at the University of Pennsylvania, Philadelphia, PA USA {alicek1, scthailes, mya}@seas.upenn.edu

Digital Object Identifier (DOI): see top of this page.

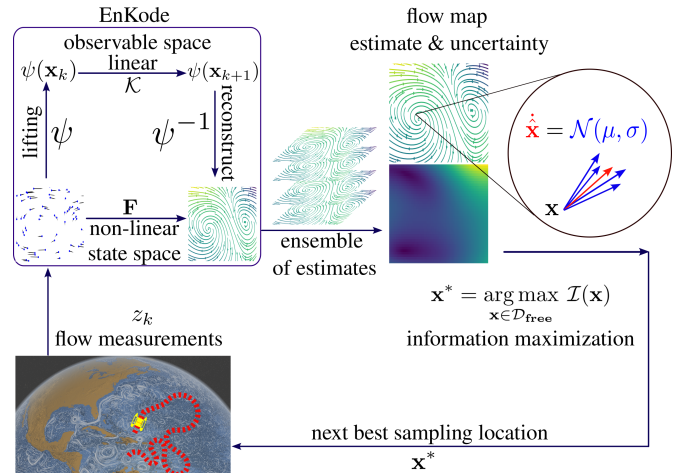


Fig. 1: EnKode modeling and active sensing scheme. Flow measurements are acquired by a robot, and fed into EnKode, which combines ensemble methods and Koopman operator theory to model unknown nonlinear ordinary differential equations with model uncertainty quantification. Measurements are encoded via lifting functions into a space where dynamics are linear, propagated forward in time by the estimated Koopman operator, and reconstructed to produce a flow estimate and uncertainty map. The next best sampling location is that with the greatest epistemic uncertainty, a measure of information, providing a feedback loop for the next best sampling location.

Koopman in 1931, is a principled and observational bias based physics-informed method [11], for estimating the dynamics of nonlinear systems [12]–[14]. This is accomplished by a coordinate transform via observables that lift the nonlinear system into a space where the dynamics are linear. The evolution of an observable can be considered an evolution of a hypersurface [15], meaning the linearity offered by KOT allows for high quality predictions in unsampled regions. Therefore, it can be insightful to apply KOT to the task of modeling flows, which are nonlinear ordinary differential equations.

In this letter, we apply Koopman-based methods to enhance the efficacy of estimating flows and modeling uncertainties where data are adaptively sampled by a robot. This is a different problem to [13], [16]–[22], where the focus is on extracting dynamics from large spatiotemporal datasets. Our contributions are as follows. We present a framework, called EnKode, that is used for active modeling of unknown flows with sparse data. Koopman theory is used for sample efficient modeling of flows. We devise a novel measure of flow model uncertainty which governs the active learning strategy, iteratively guiding a data-gathering robot towards informative sampling locations. We apply our methods to various fluid flows, and compare flow modeling errors when a robot actively samples, as opposed to uniform back-and-forth coverage. We

also make comparisons with the commonly used Gaussian Process regression (GP) model representation as a baseline.

II. RELATED WORK

To date, GPs [23] have been widely used for modeling fluid flows from sparse measurements [3], [4], [24]–[26]. The wide adoption of GPs for estimating fluid flows is primarily due to its ease of use, the uncertainty estimation it offers, and the ability to make predictions in unsampled regions of the flow. However, a well-known drawback of such methods is the need to pre-select a mean and covariance kernel, where the choice governs the quality of the predictions. In addition, hyperparameters must be pre-defined. Despite these drawbacks, many robotics flow modeling works use GPs.

Additional works have demonstrated success in modeling fluid flows in robotics using other regression techniques. Kernel embeddings that enforce the same incompressible kernel methods derived in [24] are used in [2], combining ensemble forecasts with sensor measurements to estimate real ocean currents. A linear combination of RBFs are used in [5] to model ocean currents. In [27], a single singularity (either source or sink) is assumed to exist, inducing regional fluid motion, and eight flow model parameters are estimated via least squares based on measurements obtained by a robot.

While these dynamics-agnostic regression methods have shown decent prediction capabilities, they are not operator-theoretic methods that model a linear functional form of dynamics. Dynamics are estimated by lifting the system into a space in which the evolution of the system is linear. Beyond prediction, this linearity enables linear analysis [13], control [28], and extraction of physically interpretable dynamics, such as modes [13] and coherent sets in [29]. While kernel methods fit a linear model in feature space for regression, linear analysis tools and control cannot be applied, as the mapping from inputs to targets is nonlinear. Therefore, using KOT, an operator-theoretic method, to model flows with limited observations could be both more effective and favorable, but to the authors’ knowledge has not been investigated yet.

In addition to dealing with nonlinearities, the evolution of functions of the states, called observables, can be considered an evolution of hypersurfaces [15], meaning that the linearity offered by KOT allows for high quality predictions in unsampled regions. An example of improvements in sample efficiency is shown in [30] where KOT methods were utilized for learning dexterous manipulation skills. They observed an improvement in sample efficiency in comparison to their non-Koopman baselines. In our work, we are interested in investigating whether Koopman-based models make high quality predictions in unsampled flow regions.

Koopman theory has been applied to other areas in robotics, many of which involve modeling the dynamics of a robot for improved control [31]–[35], rather than the dynamics of a robot’s environment. To the best of our knowledge, our work is the first to use Koopman methods for adaptive sampling of flows. Of all these Koopman-based works listed above, [35] is the most similar in that the dynamics of quadcopters are parameterized by Koopman operators and learnt online to stabilize during free-fall. We are similarly interested in

learning system dynamics online, because power and resource constrained robots acquiring real world data is resource intensive and can become intractable for large-scale environments [36], [37]. However, to learn environmental dynamics online, prediction uncertainty must be quantified to guide robots to information rich regions.

Numerous techniques inspired by information theory, such as mutual information [38], have been adopted to define state estimation uncertainty in robotics. Assuming that maximizing epistemic uncertainty is a proxy for maximizing information gain, an agent is able to query the environment and acquire more information about the state that a robot is most uncertain about [39].

We introduce a novel method for estimating the informativeness of a sampling location when modeling flow dynamics. Existing uncertainty estimation for KOT methods are shown in [40], where the Fisher information of each element of the Koopman operator is estimated, based on historical dynamics data gathered prior to deployment. This is used to determine the robot control policy, providing quadcopter trajectories which maximize information gained. We do not assume access to prior information. Instead, our techniques are inspired from active learning methods [41] and the concept of *query by disagreement* [42]–[44]. We train an ensemble of models online, and a robot samples in spatial locations corresponding to the largest disagreement in an ensemble of these models [45]. This method does not require computations of variables in the observable space, and intuitively provides the uncertainty as the variance across the outputs of a set of models. Our novel Koopman-based sparse modeling, uncertainty, and adaptive sampling methods are detailed in the sections that follow.

III. PROBLEM FORMULATION

A. Connections Between Flows & Koopman Operators

We consider fluid systems that are assumed to be time-invariant, and can be represented by a continuous autonomous dynamical system of the form:

$$\dot{\mathbf{x}} = \mathbf{F}(\mathbf{x}) \quad (1)$$

on a smooth manifold $\mathcal{M} \in \mathbb{R}^2$, with a smooth and Lipschitz vector field $\mathbf{F} : \mathcal{M} \rightarrow \mathcal{M}$, and $\Phi(\mathbf{x}_0, k) = \mathbf{x}(k)$ is the flow of \mathbf{F} . We define \mathcal{F} as the observable space, which is the possibly infinite-dimensional space of scalar complex valued observables or observable functions $\varphi : \mathcal{M} \rightarrow \mathbb{C}$. An observable is a scalar-valued lifting function measuring a relevant property of the dynamical system. It provides a coordinate transformation into a possibly infinite-dimensional Koopman invariant space, such that the system’s originally nonlinear dynamics behaves linearly.

Finally, while \mathbf{F} acts on $\mathbf{x} \in \mathcal{M}$, the linear Koopman operator $\mathcal{K} : \mathcal{F} \rightarrow \mathcal{F}$ acts on observable functions φ by composition with the evolution rule, \mathbf{F} . This is defined by:

$$\mathcal{K}\varphi = \varphi \circ \mathbf{F}, \quad (2)$$

where \circ is the function composition.

EnKode estimates a discrete dynamics model, $\mathbf{x}_{k+1} = \mathbf{F}(\mathbf{x}_k)$, that is sampled from the underlying process, (1). The

discrete form of (2) is: $\mathcal{K}_{\Delta t}\varphi = \varphi(\mathbf{x}_{k+1})$. When $\mathcal{K}_{\Delta t}$ acts on observable functions of the system at time k , the observables move along the solution curve to time $k+1$.

According to [12]–[15], Koopman eigenfunctions, ψ , are a special set of observables such that the following holds:

$$\psi(\mathbf{x}_{k+1}) = \mathcal{K}_{\Delta t}\psi(\mathbf{x}_k) = \lambda\psi(\mathbf{x}_k) \quad (3)$$

where \mathbf{x}_k represents the state at time k , \mathbf{x}_{k+1} is the state at time $k+1$, and λ is an eigenvalue of the Koopman operator.

With the above, we formulate our problem as follows.

Problem 1. Given a robot operating in a domain \mathcal{D} , and a sampling budget N_{total} , the robot must model an *a priori* unknown velocity flow field \mathbf{F} :

$$\mathbf{x}_{k+1} = \mathbf{F}(\mathbf{x}_k),$$

where $\mathbf{x} = [x, y]^T \in \mathcal{D}$, and $\mathbf{F} : \mathbb{R}^2 \rightarrow \mathbb{R}^2$ based on zero-mean noisy in-situ flow measurements \mathbf{z} of variance σ :

$$\mathbf{z}(\mathbf{x}) = \mathbf{F}(\mathbf{x}) + \omega, \quad (4)$$

where $\omega \sim \mathcal{N}(0, \sigma^2)$ is an additive noise. In the absence of in-situ flow measurements, $\Delta\mathbf{x} = \mathbf{F}(\mathbf{x})\Delta t$ provides a proxy of the flow dynamics, where $\Delta\mathbf{x} = \mathbf{x}_{k+\Delta t} - \mathbf{x}_k$ is the change in robot position, between time Δt .

Information used to estimate a flow field are gathered iteratively by selecting the next best sampling location:

$$\mathbf{x}^* = \arg \max_{\mathbf{x} \in \mathcal{D}_{\text{free}}} \mathcal{I}(\mathbf{x}), \quad (5)$$

where \mathcal{I} is measure of informativeness of sampling from a flow field location, and $\mathcal{D}_{\text{free}}$ are obstacle free and previously unsampled regions.

IV. METHODOLOGY

A. Estimating the Observables with EnKode

EnKode is based on (3), and finds an estimate of observables that linearize the dynamics, which is when eigenfunctions live in the span of the observables. As mentioned previously, the lifted space is possibly infinite-dimensional. However, dealing with infinite dimensions is computationally intractable. Therefore, like many data-driven Koopman theory works [20], [46]–[49], we aim to find a finite approximation of both the eigenfunctions $\hat{\psi}$ and the associated Koopman operator, $\hat{\mathcal{K}}$.

Training Data. The training data of size N is organized into two matrices: inputs, $\mathbf{X}_k \in \mathbb{R}^{N \times 2}$ and corresponding labels, $\mathbf{X}_{k+1} \in \mathbb{R}^{N \times 2}$. At the start of an experiment $N = 1$, *i.e.*, we have a single training sample in the dataset. The flow is then estimated; the next sampling location is determined; and a new sample is added to the dataset, making $N = 2$. This continues until the end of the experiment, where the robot is allowed a budget of N_{total} samples. For the n -th pair of input and label, $\mathbf{x}_k^n \in \mathbf{X}_k$ represents the robot’s *initial* position at adaptive sampling iteration n , and $\mathbf{x}_{k+1}^n \in \mathbf{X}_{k+1}$ represents the robot’s *next* position, after it is evolved by the underlying flow dynamics. We assume the flow to be time-invariant, similar to many works including [2], [50], and assume the time between any \mathbf{x}_k^n and \mathbf{x}_{k+1}^n pair is Δt . We refer to *samples* as the size of the training data.

Providing Structure for Observables. For EnKode, \mathbf{X}_k is lifted via a feature map defined by ν Fourier features. Each Fourier basis function is defined by a frequency vector, $\mathbf{w}_i \in \mathbb{R}^2$, and phase shift, b_i , for $i = 0, \dots, \nu$. These parameters are learnable model weights, and are unknown prior to the modeling task and are initialized randomly. There are 3ν learnable parameters for EnKode. They are optimized online as the robot collects additional observations. The feature map $\hat{\Psi}$ is represented as:

$$\hat{\Psi}(\mathbf{X}_k) = [\mathbf{X}_k, \mathbf{cos}(\mathbf{w}_0^T \mathbf{X}_k + b_0), \mathbf{cos}(\mathbf{w}_1^T \mathbf{X}_k + b_1), \dots, \mathbf{cos}(\mathbf{w}_\nu^T \mathbf{X}_k + b_\nu)], \quad (6)$$

where cosine is vector-valued and applied element-wise to its inputs. We choose Fourier features because we empirically find that they capture the periodic and vortex-like flow dynamics well. Additional results are shown in [29].

Loss Function. Based on this definition of the feature map, we can then find an estimate of the Koopman operator, $\hat{\mathcal{K}}$, using its relationship with $\mathcal{K}_{\Delta t}$, in (3). We jointly learn both the feature map $\hat{\Psi}$ and the linear operator, $\hat{\mathcal{K}}$, via stochastic gradient descent, using PyTorch, trained with the Adam optimizer and autograd, where we minimize the following loss function over $\theta = \{\omega, b, \hat{\mathcal{K}}\}$:

$$\min_{\theta} \|\hat{\Psi}(\mathbf{X}_{k+1}) - \hat{\mathcal{K}}(\hat{\Psi}(\mathbf{X}_k))\|_2. \quad (7)$$

The mean squared error (MSE) is used to compute the loss, \mathcal{L} . This loss term is to ensure linearity of $\hat{\mathcal{K}}$ applied to all the lifted measurements. To prevent over-fitting, we apply L2 regularization on $\hat{\mathcal{K}}$, and weights θ via PyTorch’s Adam weight decay.

Note that in (6), the measurements are appended to the set of Fourier basis. This is done for two reasons. First, it prevents model weights from approaching zero, as a feature map with weights of zero magnitude satisfies the loss (7). Also, the system state at the next timestep, can then be found with the identity observable $\psi(\mathbf{X}_k) = \mathbf{X}_k$, without relying on any mapping for reconstruction, similar to [48].

B. EnKode Flow Prediction and Uncertainty Estimation

Using the linearity offered by Koopman Operators, the flow field in both sampled and unsampled regions of the flow is estimated by EnKode, and defined by the learnt lifting functions and Koopman Operator from (3). Let us define the model output by EnKode as a flow field for $\mathbf{x} \in \mathcal{D}$:

$$\hat{\mathbf{x}}_{k+1} = \hat{\mathbf{F}}(\mathbf{x}_k) \simeq \hat{\Psi}^{-1}(\hat{\mathcal{K}}\hat{\Psi}(\mathbf{x}_k)). \quad (8)$$

The flow is estimated for test points $\mathbf{X}' \in \mathcal{D}$. The forward propagated identity observable in (6) is used to construct the flow field. The resolution of the estimated velocity field is variable, and can be defined depending on the application. To make flow predictions, we aggregate the output of M models with the same structure, *i.e.*, identical ν , but model weights are initialized to non-identical sets of θ , as in [45], to obtain an average flow of M models, where M is the number of members of the ensemble.

To obtain the estimation uncertainty, we compute the variance of M flow vectors for all $\mathbf{x}' \in \mathbf{X}'$. Let $\mathbf{V}(\mathbf{x}')$ represent

the set of M 2D vector flow estimates $\mathbf{v}_m(\mathbf{x}')$ at a location \mathbf{x}' . We quantify uncertainty, \mathcal{U} , as the weighted sum of the variance of the L2 norm and circular variance:

$$\mathcal{U}(\mathbf{x}') = \text{Var}[\|\mathbf{V}(\mathbf{x}')\|_2] + \beta \text{Var}_\Theta[\mathbf{V}(\mathbf{x}')], \quad (9)$$

where $\text{Var}_\Theta[\mathbf{V}(\mathbf{x}')] = 1 - \bar{R}$; $\bar{R} = R/M$, and $R^2 = (\sum_j^M \cos(\theta_j))^2 + (\sum_j^M \sin(\theta_j))^2$, as defined by Fisher in [51], θ is the angle of the vector from a universal x -axis, β is a hyperparameter that weights the importance of the two forms of uncertainty in the modeling task. Any number of ensemble models can be used—we show a sensitivity analysis based on the number of ensemble models used in Sec. VI. Unless specified, we use $M = 10$.

Algorithm 1 Active Learning Loop

Require: $\mathcal{D}, \nu, M, \theta, N_{total}, \mathbf{X}_k = [\mathbf{x}_k^0], \mathbf{X}_{k+1} = [\mathbf{x}_{k+1}^0]$
for $N \leftarrow 1$ to N_{total} **do**
 for m in M **do**
 for $(\mathbf{x}_k, \mathbf{x}_{k+1})$ in $(\mathbf{X}_k, \mathbf{X}_{k+1})$ **do**
 Predict, $\hat{\mathbf{x}}_{k+1} \leftarrow \text{EnKode}(\mathbf{x}_k, \theta)$
 Compute loss, $\mathcal{L} \leftarrow \text{MSELoss}(\hat{\mathbf{x}}_{k+1}, \mathbf{x}_{k+1})$
 Compute gradients, $\nabla_\theta \mathcal{L}$
 Update weights for $\hat{\Psi}$ and \hat{K}
 end for
 Predict vector field $\hat{\mathbf{F}}_m(\mathbf{x})$
end for
 Compute variance over M vector fields, \mathcal{U}
 Get next best sampling location, $\mathbf{x}^* = \arg \max_{\mathbf{x} \in \mathcal{D}_{\text{free}}} \mathcal{U}(\mathbf{x})$
 Acquire training sample at \mathbf{x}^* , $(\mathbf{x}_k^N, \mathbf{x}_{k+1}^N)$
 Append new inputs, $\mathbf{X}_k \leftarrow [\mathbf{X}_k, \mathbf{x}_k^N]$
 Append new targets, $\mathbf{X}_{k+1} \leftarrow [\mathbf{X}_{k+1}, \mathbf{x}_{k+1}^N]$
end for

C. Active Learning Loop

Algorithm 1 describes the active learning loop:

ACTIVE SENSING or learning allows the robot to query the environment from specific locations that benefit the map estimate, depending on the next best sensing location criterion. At the very start of the experiment, $N = 1$, and an initial random sensing location is selected.

ENCODE UPDATES are performed by incorporating the actively sampled observations into the training data. Model weights are updated from the previous model weights.

PLANNING for the next best sampling location is determined by the concept of *query by disagreement* [41]. For this, we assume that minimizing uncertainty is a proxy for maximizing information gain \mathcal{I} in 5, as in [43]. The most informative sampling location is that with greatest disagreement in prediction in the M models. The most informative point $\mathbf{x}^* \in \mathcal{D}_{\text{free}}$, given model prediction uncertainty \mathcal{U} is:

$$\mathbf{x}^* = \arg \max_{\mathbf{x} \in \mathcal{D}_{\text{free}}} \mathcal{U}(\mathbf{x}). \quad (10)$$

We note the sampling strategy is myopic and does not consider distance travelled. This is done intentionally to remove all other independent variables, allowing us to systematically assess whether sampling in spatial locations with maximum uncertainty estimated by EnKode reduces modeling error.

V. EXPERIMENTS

We conduct various experiments with $N \leq 36$. First, we use adaptive sampling to model vector fields using EnKode without hyperparameter optimization, versus GP with hyperparameter optimization (w/ OPT), and GP without hyperparameter optimization when number of samples $N < 10$ (w/o OPT). We then make comparisons of adaptive versus uniform sampling, akin to back-and-forth patterns for information gathering commonly adopted in real-world applications. We evaluate the performance of EnKode on three different fluid flow domains: Bickley Jet, the Lid-driven Cavity flow with an obstacle, and real ocean currents from the National Oceanic and Atmospheric Administration, from ERDDAP [52]. Finally, we assess the effect of three parameters of interest (number of Fourier features ν in (6), number of ensemble models M , weighting β defined in (10).

The following metrics are used to assess EnKode's modeling and adaptive sampling performance:

- 1) *End-to-End Point Error (EPE)*. We take inspiration from optical flow metrics, which apply to our flow estimation task. For spatial plots, for every $\mathbf{x} \in \mathbf{X}'$, we compute the Euclidean norm of point-wise EPE: $\|\dot{\mathbf{x}} - \hat{\mathbf{x}}\|_2$ [53].
- 2) *Cosine Similarity (CS)*. For CS, we compute point-wise errors across the domain $CS = \frac{\dot{\mathbf{x}} \cdot \hat{\mathbf{x}}}{\|\dot{\mathbf{x}}\|_2 \|\hat{\mathbf{x}}\|_2} \in [-1, 1]$, and report the average CS across the entire domain. The closer the CS to 1, the more aligned the vector. A value of -1 signifies vectors are oriented in opposite directions.
- 3) *Magnitude Error (ME)*. While EPE may capture a notion of magnitude error, we additionally evaluate on ME, which removes any angular error dependence. ME is defined as $\left| \|\dot{\mathbf{x}}\|_2 - \|\hat{\mathbf{x}}\|_2 \right|$.

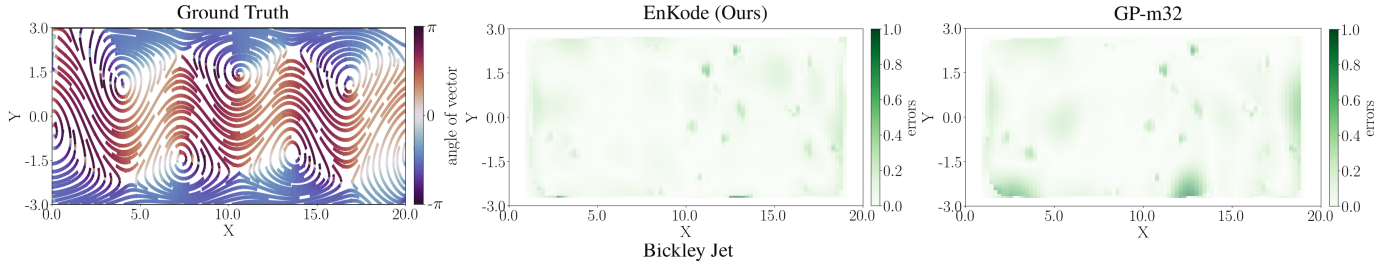
Every CS, EPE, and ME curve and sensitivity results represent an aggregate of 10 experimental trials. For the GP baseline, we use GPy [54] and their L-BFGS hyperparameter optimization functionality, either performed at every sampling iteration (w/ OPT), or at every sampling iteration $N < 10$ samples (w/o OPT). We make comparisons with two commonly used kernels: (1) Radial Basis Function (GP-rbf), also known as the squared exponential function: $k(\mathbf{x}_i, \mathbf{x}_j) = \exp\left(-\frac{d(\mathbf{x}_i, \mathbf{x}_j)^2}{2l^2}\right)$, where d denotes Euclidean distance between its inputs, and l is a lengthscale, and (2) Matérn32 (GP-m32): $\sigma_f^2 \left(1 + \sqrt{\frac{3d(\mathbf{x}_i, \mathbf{x}_j)^2}{l^2}}\right) \exp\left(-\sqrt{\frac{3d(\mathbf{x}_i, \mathbf{x}_j)^2}{l^2}}\right)$. The GP has 4 learnable parameters: noise variance σ_n , signal variance σ_f , and length-scale parameters for each dimension l_1, l_2 . Next, we define variables with standard GP notation, making connections with our EnKode variables wherever possible. GP training inputs are $\mathbf{X}^{GP} = \mathbf{X}_k$. The labels are $y^{GP} = \mathbf{X}_{k+1}$. A GP kernel $K(\mathbf{X}', \mathbf{X}^{GP})$ denotes a matrix of covariances evaluated at all pairs of test points \mathbf{X}' and training points \mathbf{X}^{GP} . Given a grid of initial position as input, \mathbf{X}' , the GP prediction of the next position, $\mathbf{y} = K(\mathbf{X}', \mathbf{X}^{GP})[K(\mathbf{X}^{GP}, \mathbf{X}^{GP}) + \sigma_n^2 I]^{-1} \mathbf{y}$. Since [55] demonstrates similar uncertainty quantification between ensemble GPs and standard GPs, and by construction, standard GPs offer prediction uncertainty, we use standard GP uncertainty to determine the next best sampling location: $\mathbf{x}^* = \arg \max_{\mathbf{x} \in \mathbf{X}'} \Sigma(\mathbf{X}', \mathbf{X}')$ where $\Sigma(\mathbf{X}', \mathbf{X}') = K(\mathbf{X}', \mathbf{X}') -$

TABLE I: PERFORMANCE METRICS FOR ACTIVE SAMPLING UP TO $N \leq 36$ WITH ENCODE AND GP.

N	Bickley						Cavity						Ocean					
	CS (\uparrow)			ME (\downarrow)			CS (\uparrow)			ME (\downarrow)			CS (\uparrow)			ME (\downarrow)		
	EnK	GP-m32	GP-rbf	EnK	GP-m32	GP-rbf	EnK	GP-m32	GP-rbf	EnK	GP-m32	GP-rbf	EnK	GP-m32	GP-rbf	EnK	GP-m32	GP-rbf
9	0.256	0.021	-0.037	0.012	0.012	0.013	0.284	0.608	0.323	0.063	0.062	0.073	0.234	0.440	0.319	0.074	0.017	0.017
16	0.456	0.272	0.060	0.010	0.011	0.013	0.573	0.604	0.601	0.051	0.057	0.065	0.385	0.354	0.474	0.024	0.018	0.016
25	0.644	0.566	0.148	0.008	0.008	0.015	0.668	0.649	0.636	0.039	0.055	0.054	0.531	0.503	0.479	0.013	0.016	0.017
36	0.791	0.715	0.231	0.005	0.007	0.015	0.728	0.657	0.638	0.030	0.051	0.054	0.639	0.599	0.510	0.011	0.013	0.016

TABLE II: PERFORMANCE METRICS FOR UNIFORM SAMPLING UP TO $N \leq 36$ WITH ENCODE AND GP.

N	Bickley						Cavity						Ocean					
	CS (\uparrow)			ME (\downarrow)			CS (\uparrow)			ME (\downarrow)			CS (\uparrow)			ME (\downarrow)		
	EnK	GP-m32	GP-rbf	EnK	GP-m32	GP-rbf	EnK	GP-m32	GP-rbf	EnK	GP-m32	GP-rbf	EnK	GP-m32	GP-rbf	EnK	GP-m32	GP-rbf
9	0.017	0.030	-0.032	0.012	0.012	0.013	0.410	0.596	0.551	0.063	0.063	0.064	0.428	0.526	0.513	0.032	0.014	0.014
16	0.204	0.185	0.119	0.012	0.012	0.013	0.633	0.633	0.626	0.059	0.059	0.063	0.437	0.560	0.523	0.021	0.013	0.014
25	0.322	0.267	0.243	0.009	0.010	0.013	0.643	0.658	0.642	0.042	0.042	0.058	0.498	0.578	0.524	0.014	0.013	0.014
36	0.463	0.471	0.324	0.007	0.005	0.013	0.769	0.780	0.654	0.025	0.024	0.042	0.621	0.587	0.527	0.011	0.013	0.013

**Fig. 2:** Pixel-wise EPE after actively modeling the flow of the Bickley Jet, for $N_{total} = 36$. Overall EnCode error is lower than that of GP-32 w/ OPT. There are localized regions with errors for the GP that do not appear in the EnCode estimate.

$K(\mathbf{X}', \mathbf{X}^{GP})[K(\mathbf{X}^{GP}, \mathbf{X}^{GP}) + \sigma_n^2 I]^{-1} K(\mathbf{X}^{GP}, \mathbf{X}')$. The location corresponds to $\mathbf{x}' \in \mathbf{X}'$ with maximum uncertainty, given by the diagonal entries of Σ .

VI. RESULTS AND DISCUSSION

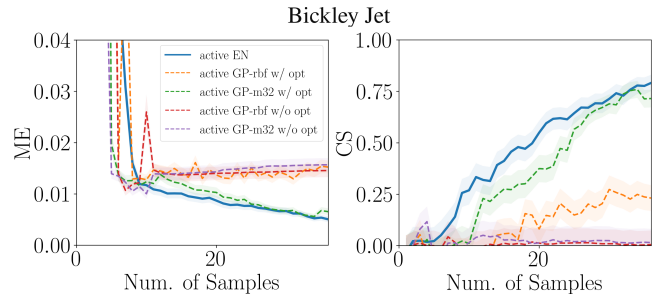
A. Performance Overview

Overall, the proposed Koopman based modeling, uncertainty quantification, and adaptive sampling scheme is suitable for learning unknown flows online. When actively modeling flows, EnCode achieves either comparable or higher CS and lower ME errors by the end of the sampling task, in comparison to the GP with or without hyperparameter optimization. This is demonstrated by the errors in Table I, for all flows. EnCode errors converge more stably with increasing number of samples, compared to the GP. Active sampling is preferred over uniform sampling when flows are dominated by more complex structure, and less uniform flow (uni-directional), e.g., Bickley Jet. This is observed when comparing Table I with Table II for each flow system. In general, when restricted to very few samples (on the order of 9–16), uniform sampling is preferable, as uniformly distributed samples capture the general flow structure better. Unless stated, we use $\nu = 64$, for all flow models. Due to space limitations, we show qualitative EPE, and tabulate and plot quantitative ME and CS for varying N .

B. Bickley Jet

The Bickley Jet is a complex flow, exhibiting a thin jet traversing from left to right and oscillating along the center line of the domain, inducing counter rotating vortices above and below this stream.

This experiment demonstrates the effectiveness of combining Koopman theory and our uncertainty measure for active sampling. In comparing Table I with Table II, we see that active sampling is better than uniform sampling for both EnCode and the GP. Furthermore, when actively sampling, Table I shows that CS is higher for EnCode in comparison to either GP, showing greater angular alignment of the estimated velocity field for any number of samples. ME for EnCode is lower or comparable to either GP. Active sampling spatial errors are shown in Fig. 2 with 36 samples. There are regions with high errors for the GP that do not exist when actively sampling and modeling with EnCode. Finally, trends in Fig. 3 show that EnCode metrics are better than both GP w/ OPT.

**Fig. 3:** Errors when actively modeling Bickley Jet. ME values closer to 0 are desired, while CS closer to 1 are desired. For $N \geq 10$, ME is lower and CS is higher when actively sampling with EnCode.

C. Lid-Driven Cavity with Obstacle

To add complexity to the standard Lid-Driven Cavity flow, we embed an obstacle (cross shape) in the middle of the cavity. The bulk of the flow in this domain is a large clockwise

rotating vortex. The obstacles, namely the cross and walls, give rise to smaller vortex structures—it can be challenging to capture features with different length scales.

Unsurprisingly, uniform sampling in Table II is preferred over active sampling in Table I, as the flow structure is uniform across the majority of the domain. When uniformly sampling, GP-m32 performs better than EnCode which performs better than GP-rbf. However, Fig. 5 shows that when actively sampling, EnCode CS and ME performance exceeds either GP after 20 samples have been collected, as Eq. (10) guides the robot to sample around the embedded cross in Fig. 4. Fig. 4 better illustrates how EnCode is able to capture the regions around the obstacle that exhibits smaller clockwise rotating vortices, while the GP cannot. In addition to showing that active sampling with EnCode performs better compared to the GP baseline, we also note that this is a successful demonstration of EnCode modeling obstacle-laden flow.

D. Real Ocean Currents

In comparison to the previous two flows, ocean currents exhibit less symmetry. A good model should be able to capture features with varying degrees of magnitude and vorticity, and not smooth out the features with smaller magnitudes.

After acquiring 20 samples selected via adaptive sampling, EnCode performs better than both GPs, as observed in Fig. 6. While active sampling with GP can occasionally outperform EnCode uniform and active sampling, the error fluctuations are undesirable, possibly capturing the GP sensitivity to training data and hyperparameter selection. By the end of the active sensing task, $N = 36$, active sampling is better than uniform sampling for both EnCode and GP, when comparing results across I and II. For uniform sampling in II, the initial well-performing GP is likely because the grid of samples represent the general flow of the domain. For a more consistent performance when modeling ocean currents, EnCode should be adopted with the active sampling scheme. Again, Table I further confirms that actively sampling with EnCode is effective. EnCode performs better than both GP models for both metrics when modeling with $N \geq 25$.

Overall, these experiments demonstrate that the uncertainty metric we define for active sampling is effective, not only for simulated data, but also using real ocean model data. Fig. 7 shows a comparison between pixel-wise errors and uncertainty after sampling at 20 locations, demonstrating the effectiveness of the informativeness measure in (10). Furthermore, the results highlight that the EnCode uncertainty estimation is more meaningful as it more closely represents the prediction error compared to that of the GP baseline.

E. Sensitivity Analyses

Information Weighting, β . Table III shows the effect of the weighting in Eq. (9). A small β value places more importance on sampling in regions with high magnitude variance, and a large β value encourages sampling in regions with high angular variance. We observe that lower ME errors are obtained when β is more heavily weighted towards one type of variance. The best CS value is obtained when $\beta = 10$, while the best

ME value is obtained when $\beta = 0.1$. However, in general, there is no significant trend when β is varied.

Number of Fourier Features, ν . Given a fixed number of optimization iterations, there is an ideal number of Fourier features used to model the ocean flow as shown in Table III. In this experiment, we optimize over Eq. (7) with a fixed number of iterations, and an 8×8 uniform grid of samples.

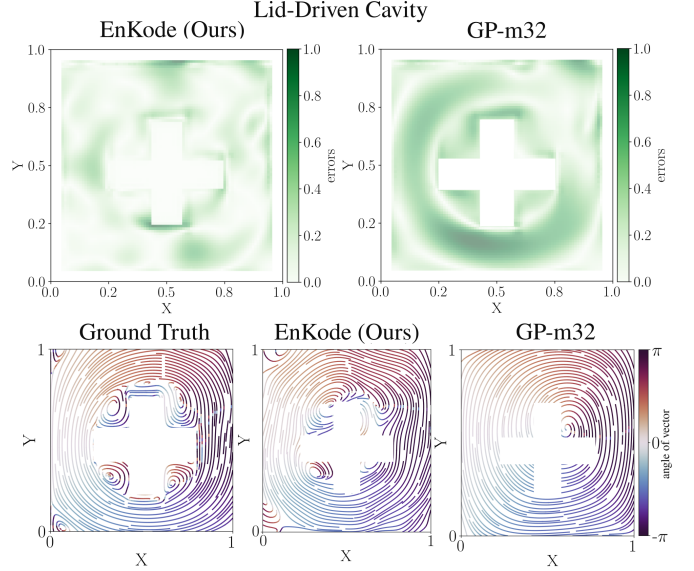


Fig. 4: TOP. Pixel-wise EPE for Lid-Driven Cavity with Obstacle. BOTTOM. Corresponding streamlines. When actively sampling, EnCode captures both the bulk flow dynamics and small vortices, while the GP is able to capture the bulk flow only.

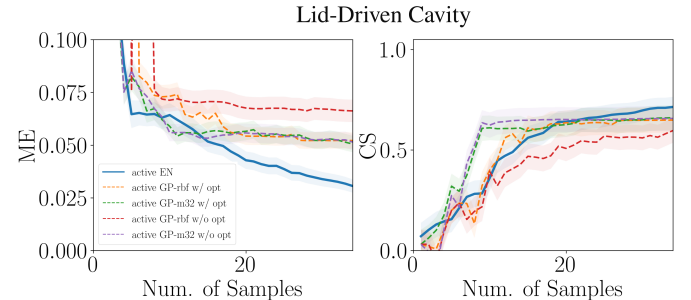


Fig. 5: Errors for modeling the Lid-Driven Cavity flow with obstacle over $N \leq 36$ samples. If active sampling is used, EnCode performs better than the GP baseline.

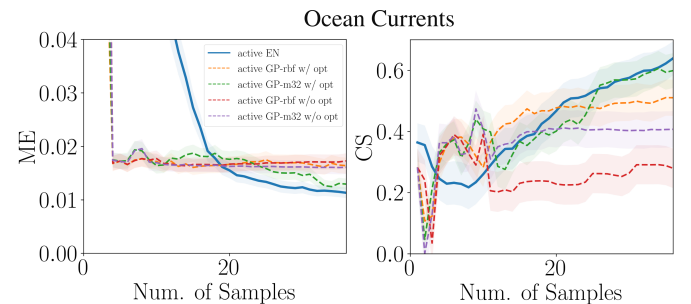


Fig. 6: Errors for modeling ocean currents over $N \leq 36$ samples. Active sampling with EnCode modeling provides reliable performance after 20 samples. GP performance occasionally exceeds EnCode, but the performance is less consistent, which is undesirable.

We evaluate the effect of increasing the number of Fourier features used to define the observables. We observe that for

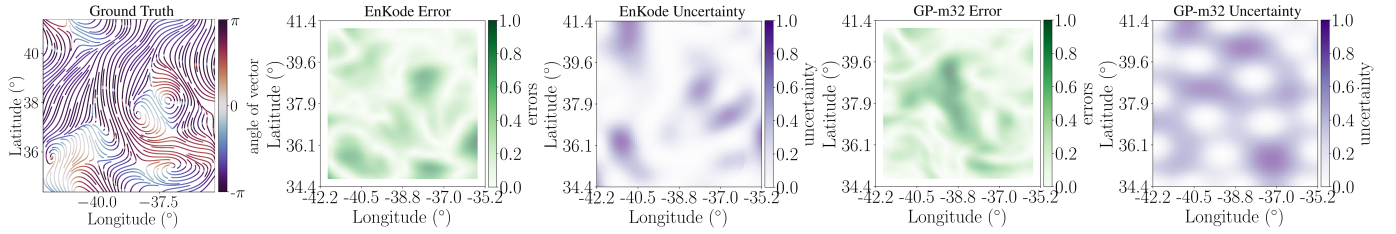


Fig. 7: Spatial plots of ground-truth flow, pixel-wise EPE, and uncertainty for EnKode and GP-m32, when modeling ocean currents. For EnKode, there is overlap in the spatial regions with high values of prediction error and uncertainty, indicating that the EnKode uncertainty estimation is meaningful for both defining the next best sampling location in an information gathering scenario, as well as serving as a suitable method for flow prediction uncertainty. On the other hand, the uncertainty values for the GP is low in sampled locations, and high elsewhere.

the number of iterations selected, 2^5 Fourier features is ideal for the lowest ME error. The CS is best with 2^6 features. The increased errors with few features is likely from a lack of expressivity; while errors from many features is likely due to a lack of estimation convergence or overfitting.

Ensemble Size, M . Table. III shows the effect of the number of ensemble members. To compute metrics in the sensitivity analyses, we accumulate the sum of errors for $N = 50$ samples. In general, the more members, the lower the ME. The CS is marginally greater with the largest number of ensemble members. There is no significant trend for CS versus M . We note that the performance across 10 experiments with 5 ensemble members is much more varied, and is a possible reason why the result for 5 ensemble members does not fit the same trend as the results for other ensemble sizes.

TABLE III: EFFECT OF β , ν AND M FOR ACTIVE SAMPLING.

β	0.1	0.5	1	2	10
CS (\uparrow)	2.326 (1.395)	2.272 (1.389)	2.362 (1.426)	2.358 (1.417)	2.385 (1.282)
ME (\downarrow)	1.023 (0.278)	1.172 (0.268)	1.133 (0.266)	1.044 (0.274)	1.051 (0.319)
ν	2^3	2^4	2^5	2^6	2^7
CS (\uparrow)	0.711 (0.044)	0.836 (0.018)	0.876 (0.009)	0.883 (0.005)	0.854 (0.014)
ME (\downarrow)	0.029 (3E-3)	0.018 (9E-4)	0.015 (6E-4)	0.016 (6E-4)	0.023 (1E-3)
M	5	10	15	20	25
CS (\uparrow)	2.338 (1.347)	2.333 (1.444)	2.366 (1.525)	2.330 (1.442)	2.447 (1.400)
ME (\downarrow)	1.105 (0.272)	1.179 (0.253)	1.162 (0.251)	1.088 (1.174)	1.019 (0.258)

VII. CONCLUSIONS

In this letter, we propose EnKode, a framework that provides flow estimation and uncertainty quantification for robotic adaptive sampling. We demonstrate the efficacy of EnKode in three different flow environments. Through these experiments, we show that KOT allows for high quality predictions in unsampled flow regions. This, along with its other benefits, including linear analysis, control, and physical interpretability, make methods grounded in operator theory favorable over dynamics-agnostic flow models. Results also show that the EnKode informativeness criterion and uncertainty quantification with ensemble methods is effective for determining the next best sampling location, as it gives rise to a reduction in the overall modeling error for three different metrics (end-to-end point error, magnitude error, and cosine similarity). When comparing sampling strategies and modeling methods, we find that for more complex flows—those with higher vortex structure like the Bickley Jet—active sampling is preferred

over uniform sampling, and EnKode modeling is preferred over GP modeling.

This work provides an opportunity for many interesting directions for future work. This work could be extended to actively learning the dynamics of higher dimensional systems, where larger amounts of data would likely be required to learn the system dynamics. In addition, in this work, the next best sampling location is intentionally point-based to assess the modeling and uncertainty estimation of EnKode. In future work, planning can be trajectory-based and also subject to travel budget and robot kinodynamic constraints. Furthermore, our approach can be extended to modeling time-varying flows, known to be periodic, as in [56], and planning with multi-robot systems.

ACKNOWLEDGEMENTS

We greatly acknowledge the support of NSF IUCRC 1939132, NSF IIS 1910308, and the University of Pennsylvania’s University Research Foundation Award. We would also like to thank Spencer Folk for data generation of the Lid-driven Cavity flow.

REFERENCES

- [1] M. Dunbabin and L. Marques, “Robots for environmental monitoring: Significant advancements and applications,” *IEEE Robotics & Automation Magazine*, vol. 19, no. 1, pp. 24–39, 2012.
- [2] K. C. To, F. H. Kong, K. M. B. Lee, C. Yoo, S. Anstee, and R. Fitch, “Estimation of spatially-correlated ocean currents from ensemble forecasts and online measurements,” in *2021 IEEE International Conference on Robotics and Automation (ICRA)*. IEEE, 2021, pp. 2301–2307.
- [3] J. Hansen and G. Dudek, “Coverage optimization with non-actuated, floating mobile sensors using iterative trajectory planning in marine flow fields,” in *2018 IEEE/RSJ International Conference on Intelligent Robots and Systems (IROS)*. IEEE, 2018, pp. 1906–1912.
- [4] R. Khodayi-mehr, P. Jian, and M. M. Zavlanos, “Physics-guided active learning of environmental flow fields,” in *Learning for Dynamics and Control Conference*. PMLR, 2023, pp. 928–940.
- [5] D. Chang, W. Wu, C. R. Edwards, and F. Zhang, “Motion tomography: Mapping flow fields using autonomous underwater vehicles,” *The International Journal of Robotics Research*, vol. 36, no. 3, pp. 320–336, 2017.
- [6] M. Michini, M. A. Hsieh, E. Forgoston, and I. B. Schwartz, “Robotic tracking of coherent structures in flows,” *IEEE Transactions on Robotics*, vol. 30, no. 3, pp. 593–603, 2014.
- [7] A. Molchanov, A. Breitenmoser, and G. S. Sukhatme, “Active drifters: Towards a practical multi-robot system for ocean monitoring,” in *2015 IEEE International Conference on Robotics and Automation (ICRA)*. IEEE, 2015, pp. 545–552.
- [8] G. A. Hollinger, A. A. Pereira, J. Binney, T. Somers, and G. S. Sukhatme, “Learning uncertainty in ocean current predictions for safe and reliable navigation of underwater vehicles,” *Journal of Field Robotics*, vol. 33, no. 1, pp. 47–66, 2016.

- [9] T. Salam and M. A. Hsieh, "Adaptive sampling and reduced-order modeling of dynamic processes by robot teams," *IEEE Robotics and Automation Letters*, vol. 4, no. 2, pp. 477–484, 2019.
- [10] S. Folk, J. Melton, B. W. Margolis, M. Yim, and V. Kumar, "Learning local urban wind flow fields from range sensing," *IEEE Robotics and Automation Letters*, 2024.
- [11] G. E. Karniadakis, I. G. Kevrekidis, L. Lu, P. Perdikaris, S. Wang, and L. Yang, "Physics-informed machine learning," *Nature Reviews Physics*, vol. 3, no. 6, pp. 422–440, 2021.
- [12] B. O. Koopman, "Hamiltonian systems and transformation in hilbert space," *Proceedings of the National Academy of Sciences*, vol. 17, no. 5, pp. 315–318, 1931.
- [13] I. Mezić, "Analysis of fluid flows via spectral properties of the koopman operator," *Annual review of fluid mechanics*, vol. 45, pp. 357–378, 2013.
- [14] M. Budišić, R. Mohr, and I. Mezić, "Applied koopmanism," *Chaos: An Interdisciplinary Journal of Nonlinear Science*, vol. 22, no. 4, 2012.
- [15] P. Bevanda, S. Sosnowski, and S. Hirche, "Koopman operator dynamical models: Learning, analysis and control," *Annual Reviews in Control*, vol. 52, pp. 197–212, 2021.
- [16] S. E. Otto and C. W. Rowley, "Koopman operators for estimation and control of dynamical systems," *Annual Review of Control, Robotics, and Autonomous Systems*, vol. 4, pp. 59–87, 2021.
- [17] M. O. Williams, I. G. Kevrekidis, and C. W. Rowley, "A data-driven approximation of the koopman operator: Extending dynamic mode decomposition," *Journal of Nonlinear Science*, vol. 25, pp. 1307–1346, 2015.
- [18] J. H. Tu, "Dynamic mode decomposition: Theory and applications," Ph.D. dissertation, Princeton University, 2013.
- [19] S. Klus, I. Schuster, and K. Muandet, "Eigendecompositions of transfer operators in reproducing kernel hilbert spaces," *Journal of Nonlinear Science*, vol. 30, pp. 283–315, 2020.
- [20] B. Lusch, J. N. Kutz, and S. L. Brunton, "Deep learning for universal linear embeddings of nonlinear dynamics," *Nature communications*, vol. 9, no. 1, p. 4950, 2018.
- [21] S. Leask, V. McDonell, and S. Samuelsen, "Modal extraction of spatiotemporal atomization data using a deep convolutional koopman network," *Physics of Fluids*, vol. 33, no. 3, 2021.
- [22] P. J. Schmid, "Dynamic mode decomposition and its variants," *Annual Review of Fluid Mechanics*, vol. 54, pp. 225–254, 2022.
- [23] C. E. Rasmussen, C. K. Williams *et al.*, *Gaussian processes for machine learning*. Springer, 2006, vol. 1.
- [24] K. M. B. Lee, C. Yoo, B. Hollings, S. Anstee, S. Huang, and R. Fitch, "Online estimation of ocean current from sparse gps data for underwater vehicles," in *2019 International conference on robotics and automation (ICRA)*. IEEE, 2019, pp. 3443–3449.
- [25] R. Berlinghieri, B. L. Trippe, D. R. Burt, R. Giordano, K. Srinivasan, T. Özgökmen, J. Xia, and T. Broderick, "Gaussian processes at the helm (holtz): A more fluid model for ocean currents," *arXiv preprint arXiv:2302.10364*, 2023.
- [26] R. C. Gonçalves, M. Iskandarani, T. Özgökmen, and W. C. Thacker, "Reconstruction of submesoscale velocity field from surface drifters," *Journal of Physical Oceanography*, vol. 49, no. 4, pp. 941–958, 2019.
- [27] J. Petrich, C. A. Woolsey, and D. J. Stilwell, "Planar flow model identification for improved navigation of small auvs," *Ocean Engineering*, vol. 36, no. 1, pp. 119–131, 2009.
- [28] H. Arbabi, M. Korda, and I. Mezić, "A data-driven koopman model predictive control framework for nonlinear flows," *arXiv preprint arXiv:1804.05291*, 2018.
- [29] T. Salam, A. K. Li, and M. A. Hsieh, "Online estimation of the koopman operator using fourier features," in *Learning for Dynamics and Control Conference, LADC 2023*, ser. Proceedings of Machine Learning Research, vol. 211. PMLR, 2023, pp. 1271–1283. [Online]. Available: <https://proceedings.mlr.press/v211/salam23a.html>
- [30] Y. Han, M. Xie, Y. Zhao, and H. Ravichandar, "On the utility of koopman operator theory in learning dexterous manipulation skills," in *Conference on Robot Learning*. PMLR, 2023, pp. 106–126.
- [31] D. Bruder, B. Gillespie, C. D. Remy, and R. Vasudevan, "Modeling and control of soft robots using the koopman operator and model predictive control," *arXiv preprint arXiv:1902.02827*, 2019.
- [32] A. Joglekar, S. Sutavani, C. Samak, T. Samak, K. C. Kosaraju, J. Smereka, D. Gorsich, U. Vaidya, and V. Krovi, "Data-driven modeling and experimental validation of autonomous vehicles using koopman operator," in *2023 IEEE/RSJ International Conference on Intelligent Robots and Systems (IROS)*. IEEE, 2023.
- [33] C. Folkestad, D. Pastor, and J. W. Burdick, "Episodic koopman learning of nonlinear robot dynamics with application to fast multirotor landing," in *2020 IEEE International Conference on Robotics and Automation (ICRA)*. IEEE, 2020, pp. 9216–9222.
- [34] L. Shi and K. Karydis, "Acd-edmd: Analytical construction for dictionaries of lifting functions in koopman operator-based nonlinear robotic systems," *IEEE Robotics and Automation Letters*, vol. 7, no. 2, pp. 906–913, 2021.
- [35] I. Abraham and T. D. Murphey, "Active learning of dynamics for data-driven control using koopman operators," *IEEE Transactions on Robotics*, vol. 35, no. 5, pp. 1071–1083, 2019.
- [36] A. K. Li, Y. Mao, S. Manjanna, S. Liu, J. Dhanoa, B. Mehta, V. M. Edwards, F. C. Ojeda, M. A. Hsieh, M. Le Men *et al.*, "Towards understanding underwater weather events in rivers using autonomous surface vehicles," in *OCEANS 2022, Hampton Roads*. IEEE, 2022, pp. 1–8.
- [37] V. Edwards, T. C. Silva, B. Mehta, J. Dhanoa, and M. A. Hsieh, "On collaborative robot teams for environmental monitoring: A macroscopic ensemble approach," in *2023 IEEE/RSJ International Conference on Intelligent Robots and Systems (IROS)*. IEEE, 2023, pp. 11 148–11 153.
- [38] A. Krause and C. Guestrin, "Nonmyopic active learning of gaussian processes: an exploration-exploitation approach," in *Proceedings of the 24th international conference on Machine learning*, 2007, pp. 449–456.
- [39] A. T. Taylor, T. A. Berrueta, and T. D. Murphey, "Active learning in robotics: A review of control principles," *Mechatronics*, vol. 77, p. 102576, 2021.
- [40] T. A. Berrueta, I. Abraham, and T. Murphey, "Experimental applications of the koopman operator in active learning for control," *The Koopman Operator in Systems and Control: Concepts, Methodologies, and Applications*, pp. 421–450, 2020.
- [41] B. Settles, "Active learning literature survey," 2009.
- [42] H. S. Seung, M. Opper, and H. Sompolinsky, "Query by committee," in *Proceedings of the fifth annual workshop on Computational learning theory*, 1992, pp. 287–294.
- [43] D. Pathak, D. Gandhi, and A. Gupta, "Self-supervised exploration via disagreement," in *International conference on machine learning*. PMLR, 2019, pp. 5062–5071.
- [44] G. Georgakis, B. Bucher, K. Schmeckpeper, S. Singh, and K. Daniilidis, "Learning to map for active semantic goal navigation," in *International Conference on Learning Representations*, 2022. [Online]. Available: <https://openreview.net/forum?id=swrMQtr6wN>
- [45] B. Lakshminarayanan, A. Pritzel, and C. Blundell, "Simple and scalable predictive uncertainty estimation using deep ensembles," *Advances in neural information processing systems*, vol. 30, 2017.
- [46] S. L. Brunton, M. Budišić, E. Kaiser, and J. N. Kutz, "Modern koopman theory for dynamical systems," *arXiv preprint arXiv:2102.12086*, 2021.
- [47] E. Yeung, S. Kundu, and N. Hodas, "Learning deep neural network representations for koopman operators of nonlinear dynamical systems," in *2019 American Control Conference (ACC)*. IEEE, 2019, pp. 4832–4839.
- [48] Q. Li, F. Dietrich, E. M. Bollt, and I. G. Kevrekidis, "Extended dynamic mode decomposition with dictionary learning: A data-driven adaptive spectral decomposition of the koopman operator," *Chaos: An Interdisciplinary Journal of Nonlinear Science*, vol. 27, no. 10, 2017.
- [49] A. Mauroy and J. Goncalves, "Koopman-based lifting techniques for nonlinear systems identification," *IEEE Transactions on Automatic Control*, vol. 65, no. 6, pp. 2550–2565, 2019.
- [50] L. Shi, R. Zheng, S. Zhang, and M. Liu, "Cooperative estimation to reconstruct the parametric flow field using multiple auvs," *IEEE Transactions on Instrumentation and Measurement*, vol. 70, pp. 1–10, 2021.
- [51] N. I. Fisher, *Statistical analysis of circular data*. cambridge university press, 1995.
- [52] R. Simons and C. John, "Erddap," 2022, monterey, CA: NOAA/NMFS/SWFSC/ERD. [Online]. Available: <https://coastwatch.pfeg.noaa.gov/erddap>
- [53] M. Otte and H. H. Nagel, "Optical flow estimation: advances and comparisons," in *Computer Vision—ECCV'94: Third European Conference on Computer Vision Stockholm, Sweden, May 2–6, 1994 Proceedings, Volume I 3*. Springer, 1994, pp. 49–60.
- [54] GPY, "GPY: A gaussian process framework in python," <http://github.com/SheffieldML/GPY>, since 2012.
- [55] M.-P. Verner Christiansen, N. Rønne, and B. Hammer, "Efficient ensemble uncertainty estimation in gaussian processes regression," *arXiv e-prints*, pp. arXiv–2407, 2024.
- [56] I. Mezić and A. Surana, "Koopman mode decomposition for periodic/quasi-periodic time dependence," *IFAC-PapersOnLine*, vol. 49, no. 18, pp. 690–697, 2016.